Research Article | Vol. 9, No. 9 / 1 September 2019 / Optical Materials Express 3729
Optical Materials EXPRESS

Performance evaluation of an implantable sensor for deep brain imaging: an analytical investigation

ROYA NAZEMPOUR,[1] CHANGBO LIU,[1] YUWEN CHEN,[1] CHENG MA,[1] AND XING SHENG[1,2,*]

[1]Department of Electronic Engineering, Beijing National Research Center for Information Science and Technology, Tsinghua University, 100084 Beijing, China
[2]IDG/McGovern Institute for Brain Research, Tsinghua University, 100084 Beijing, China
*xingsheng@tsinghua.edu.cn

Abstract: Imaging neural activities at the cellular level in the deep brain is essential to understand the structure and functions of nervous systems. Recently developed fully implantable optical sensors have the capability to capture fluorescence signals within the deep tissue; however, their potential for high-quality imaging is not clear. In this paper, we develop a simplified model to analytically study the photon transport in the biological tissue, and utilize it to understand the optical performance of an implantable fluorescence imager. Spatial resolution of the implanted imager is calculated, and imaging qualities for groups of neurons in two- and three-dimensional configurations are evaluated. The results here establish feasible solutions to design implantable optical sensors and predict their performance for biomedical applications.

1. Introduction

Unraveling the mysteries of the brain structure and functions is the key of neuroscience, and sets up the foundation of developing emerging technologies for neurological disease treatment and neuromorphic computers [1]. Methods like electroencephalography (EEG), X-ray computed tomography (CT), and functional magnetic resonance imaging (fMRI) are widely used to understand the nervous system and have realized clinical applications [2]. However, their spatial resolution is limited and has weak relevance with the cellular activities of the neuron network. Microelectrode arrays can be applied on the cortex surface or implanted into the deep brain, monitoring neuronal activities by recording extracellular and even intracellular signals [3–5]. Although such microelectrodes can achieve high spatial and temporal resolutions, it is challenging to decode a large volume of neurons (for example, $> 10^4$) at the cellular level [6].

Recently, optical methods have been extensively exploited to probe the neuronal system, not only realizing ideal spatial and temporal resolutions but also having the capability to capture numerous neurons at the same time [7,8]. In particular, the rapid development of genetically encoded fluorescent indicators enables precise signal detection for specific types of neurons [9]. Large-scale, *in vivo* imaging has been demonstrated to monitor ion (for example, Ca^{2+} [10]), neurotransmitter (for example, dopamine [11]) or direct voltage signals at the cellular level [12]. Unlike X-ray, ultrasound and magnetic field, optical imaging is plagued by the strong absorption and scattering of biological tissues in the visible range. Non-invasive, *in vivo* optical imaging can only be performed on the cortex surface or at a depth less than ~2 mm even with the aid of advanced techniques like confocal microscopy [13] and multiphoton microscopy [14,15]. While emerging tools like micro-optical sectioning tomography (MOST), CLARITY and expansion microscopy have potential to image the whole brain [16–18], currently such tools cannot be applied for living cells *in vivo* since brain tissues are sliced or engineered to become more transparent by eliminating certain components in the cell body.

#369289 https://doi.org/10.1364/OME.9.003729
Journal © 2019 Received 28 Jun 2019; revised 8 Aug 2019; accepted 9 Aug 2019; published 16 Aug 2019

Optical Materials EXPRESS

To bypass these challenges, implantable devices and systems are developed to capture optical signals in the deep brain tissue [19]. Bundles of optical fibers [20] or gradient index (GRIN) lenses [21] can be implanted into the brain, delivering light into the deep tissue and guiding fluorescence signals out to external imaging systems, which can be miniaturized for use in experimental animals [22]. Shortcomings of these systems are associated with the large lesion created by these implanted fiber bundles and GRIN lenses. In addition, the fiber bundles and GRIN lenses can only take images at a certain depth. In some scenarios, it is crucial to probe neural signals at different depths in the brain, in order to understand the connection among different brain regions and nuclei [23,24]. Recently, an implantable image sensor system is proposed to observe real-time fluorescence activities in the deep brain [25]. Conceptually illustrated in Fig. 1(a), the implantable imager combines a customized, complementary metal-oxide-semiconductor (CMOS) sensor and light-emitting diode (LED) based excitation sources, integrated onto a flexible thin-film probe and injected into the deep brain. LEDs with appropriate wavelengths are utilized to excite the neurons expressing target fluorescence dyes or proteins (for example, GCaMP6 for Ca^{2+} sensing [10]). Spatially and temporally resolved fluorescence signals are captured by the image sensor, so neuronal activities of behaving rodents can be decoded *in vivo* (Fig. 1(b)). Different from fiber bundles and GRIN lenses that coupled to external imagers, such implanted imagers directly receive optical signers from tissues on the surface, without using any lens optics or other systems for focusing. Although the imager sensor can be formed based on the-state-of-the-art CMOS technology and reach a pixel size of a few micrometers, it is unclear how these systems perform, in terms of their imaging qualities (resolution, contrast, etc.).

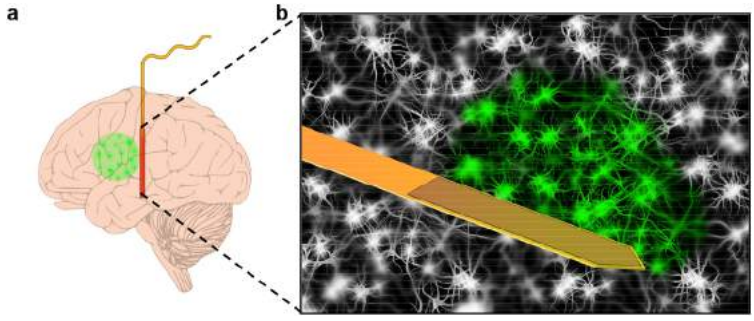

Fig. 1. (a) Schematic illustration of an implantable image sensor for fluorescence mapping in the deep brain. (b) Zoomed-in view of the sensor on a thin-film probe, capturing the fluorescence signals of neurons in the brain tissue.

In this paper, we aim to analytically understand the performance of an implanted optical imager shown in Fig. 1. Based on the photon transport in the biological tissue, we investigate the resolution limits for such an implantable imager, and numerically predict the quality of images mapping a group of fluorescent neurons in two-dimensional (2D) and three-dimensional (3D) conditions. The results are discussed, with possible solutions for performance improvements provided as research directions in the future.

2. Results

To predict the performance of the aforementioned implantable, microscale imaging sensor shown in Fig. 1, we establish a mathematical model to analyze the photon propagation in the brain. Schematically illustrated in Fig. 2(a), the thin-film probe with an image sensor is implanted into the mammalian neural tissue. On top of the imager, there is only one neuron expressing green fluorescent protein (GFP). To simplify the model, here we assume that the GFP fluorescence is isotropic and monochromatic at the wavelength of 520 nm, and the neuron is approximated by a

Optical Materials EXPRESS

sphere with a diameter of 10 μm. The CMOS sensor is also assumed to be monochromatic, having ideal photon responsivity and spectral selectivity. It means that it has a 100% photon-to-electron conversion efficiency at all receiving angles at 520 nm and no response at the GFP excitation wavelength (~480 nm). For a specific pixel in the CMOS sensor, the optical power received by the pixel can be described as [26]

$$I(x) = I_0 \frac{\exp(-\mu_{\text{eff}} L)}{L^n} \tag{1}$$

where I_0 is related to the output power emitting from the neuron (which can be normalized to 1), L is the distance from the pixel to the center of the neuron cell, and

$$L = \sqrt{x^2 + d^2} \tag{2}$$

Here d is the distance between the imager and the center of the neuron cell, and x is the distance from the pixel to the projection of the center of the neuron cell onto the sensor plane. μ_{eff} is the effective attenuation coefficient and defined as

$$\mu_{\text{eff}} = \sqrt{3\mu_a(\mu_a + \mu'_s)} \tag{3}$$

where μ_a is the absorption coefficient of biological tissue, and μ_s' is the transport scattering coefficient defined as

$$\mu'_s = \mu_s(1 - g) \tag{4}$$

where g is the anisotropy of biological tissue that has a representative value of 0.85 (highly forward scattering), and μ_s is the scattering coefficient of biological tissue. Here we apply the parameters for white matter of the brain, at 520 nm $\mu_a = 0.19$/mm and $\mu_s = 44.3$/mm [27].

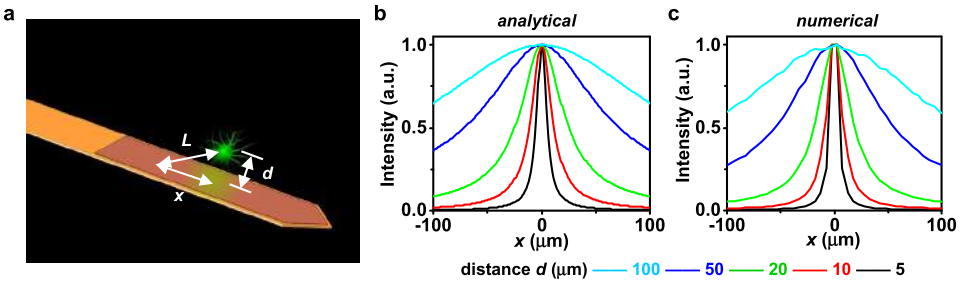

Fig. 2. (a) Schematic illustration of the optical model showing one fluorescent neuron on top of the imager, with a distance d from the imager. (b, c) Normalized fluorescence intensity profiles of the neuron detected by the imager at various distances (d = 100, 50, 20, 10 and 5 μm), based on: (b) our analytical model and (c) numerical (Monte Carlo ray tracing) simulation, respectively.

In Eq. 1, n is a geometrical parameter and dependent on the photon propagation length. For short propagation lengths (smaller than the mean free path $1/\mu_s$), photon transport can be approximated using the wave theory; for long propagation lengths (larger than the mean free path $1/\mu_s$), diffusion theory should be applied [26]. Therefore, we have

$$n = 2 \text{ for } d \ll \frac{1}{\mu_s} \tag{5}$$

and

$$n = 1 \text{ for } d \gg \frac{1}{\mu_s} \tag{6}$$

Optical Materials EXPRESS

To accommodate the situations in the intermediate region for d and satisfy Eq. 5 and 6, we describe n in a generalized form:

$$n = 2 - \exp(-\mu_s d) \tag{7}$$

Based on the above discussion and Eqs. (1)–(7), we calculate the intensity profiles for the fluorescent neuron detected by the imager at different distances, and plot the normalized data in Fig. 2(b). The results are compared with those obtained using the Monte Carlo ray tracing method based on the same simulation parameters (Fig. 2(c)) [28]. It can be observed that the analytical and numerical results show a good agreement. The discrepancies at small distances d are probably associated with the complex scattering behaviors that are difficult to model perfectly with the above equations. Nevertheless, the analytical model we develop here presents a reasonable level of accuracy to understand the photon transport in the biological tissue, and can be employed to effectively and efficiently calculate optical intensity profiles generated from large groups of neurons, which will be presented in subsequent sections.

Based on the analytical model developed above, we further evaluate the limits of the spatial resolution for the implantable sensor for imaging purposes. Schematically illustrated in Fig. 3(a), here we establish a model with two fluorescent neurons on top of the imager in the brain tissue. The two neurons are assumed to have identical fluorescence power, with the same distance d from the device surface and varied spacing Δx. Based on the above Eqs. (1)–(7) and results in Fig. 2(b), we can calculate the fluorescence intensity profile captured by the imager for each neuron. The two peaks superpose to form the resultant profile projected onto the imager. Figures 3(b)–3(e) plot representative results of normalized fluorescence intensity profiles for two neurons at various Δx (150, 90, 38, and 25 μm) and a fixed d (20 μm). When the spacing Δx decreases, the two peaks overlap and become indistinguishable. Here the resolution R is defined as the critical spacing Δx, at which the half heights of the two peaks coincide. For example, $R \approx 30$ μm for $d = 20$ μm. Based on this criterion, Fig. 3(f) plots the calculated spatial resolution limit as a function of d. R is ~8 μm for $d = 5$ μm, and monotonically increases with d. In the mammalian brain, the density of neurons varies in different brain regions, so does the performance for the imager. In some regions with densely packed neurons, the average distance between neurons is ~25 μm [29]. In these regions, the implanted imager can only resolve fluorescent neurons with $d < 20$ μm, while neurons far apart from the sensor cannot be resolved. These results provide a baseline to understand the resolution limits for the implantable imager and offer a guideline on its applicable occasions for *in vivo* fluorescence imaging.

In Fig. 4(a), we further establish a model to study a group of fluorescent neurons on top of the imager. These neurons, which are assumed to have the same luminescent power, are randomly located on a plane with a distance d from the imager. This model could emulate the imaging of a thin brain slice *ex vivo*. The neuron density is 1200 /mm^2, and the average distance between neurons is ~28 μm [30]. The implanted CMOS sensor has an active area of 400×400 μm^2. Figures 4(b)–4(f) present calculated fluorescence intensity profiles detected by the imager when the same set of neurons are positioned at various distances ($d = 5$, 10, 20, 50 and 100 μm) from the imager surface. In these contour maps, the results are normalized to (0, 1) with background signals subtracted. At small distances (for example, $d = 5$ μm), most fluorescent neurons can be well resolved, and single cell activity would be clearly observed in experimental conditions *in vivo*. When the distance d increases, the imaging starts to get blurred. In accordance with the calculations in Fig. 3, the implanted imager can only resolve fluorescent neurons with $d < 20$ μm, if the average distance between neurons is around 20–30 μm. For larger distances ($d = 50$ or 100 μm), fluorescent signals from individual neuron cannot be distinguished. Instead, what the sensor captures is superposed photon emission from multiple neurons, which represents the overall neural activity in the specific brain region. In these scenarios, the results should be similar to those photometric results obtained via an implanted fiber [31] or a photodetector [32].

Optical Materials EXPRESS

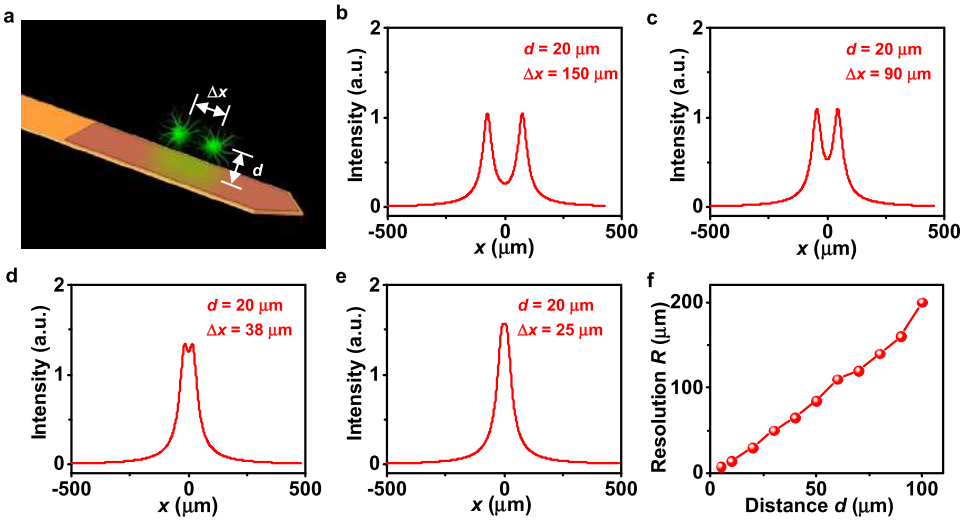

Fig. 3. (a) Schematic illustration of the optical model showing two fluorescent neurons on top of the imager, with the same distance d from the imager and a varied spacing Δx between each other. (b–e) Normalized fluorescence intensity profiles detected by the imager at various Δx (150, 90, 38, and 25 μm) and a fixed d (20 μm). (f) Calculated resolution limits R as a function of d.

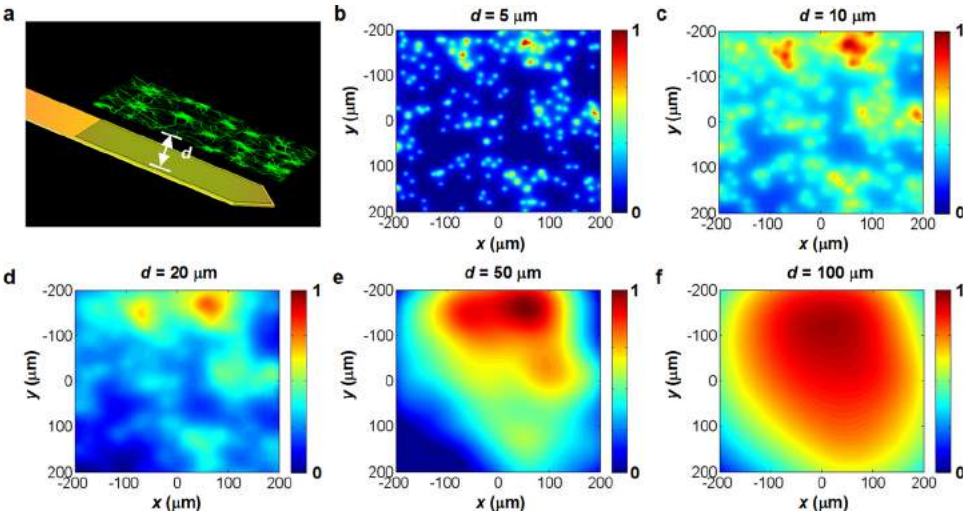

Fig. 4. (a) Schematic illustration of the optical model showing a group of fluorescent neurons on top of the imager, with the same distance d from the imager. The neurons are randomly distributed, with an areal density of ~1200 /mm^2. (b–f) Normalized fluorescence intensity profiles detected by the imager at various distances (d = 5, 10, 20, 50 and 100 μm).

Ultimately, a more realistic circumstance is to consider an implanted imager into a brain region *in vivo* with fluorescent neurons in 3D space, as we investigate in Fig. 5. The human brain has a 3D structure with a volume of ~1500 cm^3 comprising ~10^{11} neurons [33]. Therefore, the volumetric neuron density is ~70000 /mm^3. Considering this fact, we establish the 3D model with a volume of 800×800×100 μm^3 that contains ~4000 randomly distributed neurons on top of the imager (distance from 5 μm to 100 μm). First, we assume all the neurons have the same

Optical Materials EXPRESS

fluorescent intensity, as shown in Fig. 5(a). We can still apply the established mathematical model in Fig. 2 and obtain the overall fluorescence intensity profile captured by the imager, as presented in Fig. 5(d). Similar to Fig. 4, the results here are also normalized to (0, 1) with certain background signals subtracted. With fluorescent centers at different distances d from the imager surface overlaid with each other, it can be seen that the 3D model is much more complicated than the 2D one in Fig. 4. In the contour map, some neurons close to the imager ($d = 5$–10 μm) can be barely resolved. Fluorescence from neurons far away from the imager contributes to the background signal with little spatial resolution, which significantly reduces the signal-to-noise ratio and thus degrades the imaging quality.

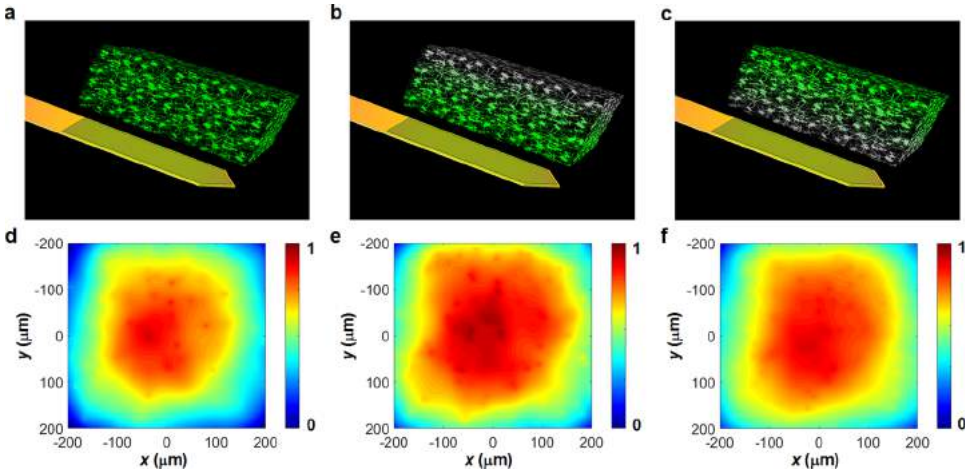

Fig. 5. (a–c) Schematic illustrations of the optical models, showing a group of fluorescent neurons in 3D space on top of the imager. The neurons are randomly distributed, with a volumetric density of ~70000 /mm^3. The fluorescence intensities for all the neurons are uniform in (a) and non-uniform in (b) and (c), depending on the positions of excitation sources. (d–f) Normalized fluorescence intensity profiles detected by the imager.

In the above analysis, the effects of excitation light sources have not been taken into account. In fact, it is highly unlikely that all the neurons have the same fluorescent intensity as shown in Fig. 5(a), due to the existence of the excitation source. Excitation can be provided by integrating microscale light emitters (for example, LEDs) on the implanted probe [25,32], or offered by illuminating the neurons on top using external sources. In these two cases, the neurons at different distances d from the imager surface receive different excitation intensity and should have different luminescent power. If we assume the neurons on the same plane still receive the same excitation power, Eq. (1) can be modified accordingly to accommodate the contribution from the excitation source. For excitation sources with the same location as the imager on the probe, we can have

$$I(x) = I_0 \frac{\exp(-\mu_{\text{eff}} L)}{L^n} \exp(-\mu_{\text{eff - ex}} d) \tag{8}$$

For external sources, we can have

$$I(x) = I_0 \frac{\exp(-\mu_{\text{eff}} L)}{L^n} \exp(+\mu_{\text{eff - ex}} d) \tag{9}$$

The two models are schematically illustrated in Figs. 5b and 5c, respectively. Here $\mu_{\text{eff–ex}}$ is the effective attenuation coefficient of the neural tissue at the excitation wavelength (~480 nm), which can be calculated based on Eqs. (3) and (4) and parameters from [27]. Calculated results

Optical Materials EXPRESS

based on the modified models are presented in Figs. 5(e) and 5(f), for the group of neurons with the same locations as those in Fig. 5(d). Obtained results are similar for different cases, since $\mu_{\text{eff}-\text{ex}}$ is small (~2 /mm). Nevertheless, the image quality shown in Fig. 2(e) is better than the other two cases, because the neurons closer to the imager possess higher luminescent power and can be more easily resolved. For the case with external excitation sources (Fig. 2(f)), the image quality is the worst because of the high background signals from fluorescent neurons far away from the imager.

3. Summary

In this work, we establish a mathematical model to investigate the optical performance of an implantable, thin-film image sensor for studying neuronal fluorescence activities in the deep brain. Based on the photon transport theory, such a simplified model presents a numerical accuracy comparable to the standard Monte Carlo ray tracing method, with clear advantages for simulating a large group of fluorescent centers in biological tissues. Our current results reveal that the imaging capability of such an implanted sensor is very limited, due to the unavailability of complex concentration optics that are necessary for high quality imaging. While fluorescent neurons close to the imager can be well resolved, those far away from the sensor cannot be focused to form a clear image and only contribute to blurred, unresolved background signals. Although it is very challenging, realizing an ultra-miniaturized and fully implanted imager is highly desirable for resolving neural activities at different depths in the deep brain. Future directions include the development of micro-machined lens systems on the imager surface to focus the signals. Other possible solutions may be the exploitation of advanced ultrathin metasurface based lens [34]. In addition, advanced image process algorithms like deconvolution [35] can be employed to enhance the contrast and possibly reconstruct better images. Furthermore, alternative red shifted fluorescence proteins [36] would possess light emission at longer wavelengths than GFPs, with reduced scattering and absorption for possibly improved imaging qualities. To summarize, the technology for implantable imagers is emerging and conceivably it will become a power tool in fundamental studies and clinical uses.

Funding

National Natural Science Foundation of China (61874064); Beijing Innovation Center for Future Chips, Tsinghua University; Beijing National Research Center for Information Science and Technology (BNR2019ZS01005); Key Laboratory of Nanodevices and Applications, Suzhou Institute of Nano-Tech and NanoBionics, Chinese Academy of Sciences (18ZS01).

Disclosures

The authors declare that they have no competing interests.

References

1. M. M. Poo, J. L. Du, N. Ip, Z. Q. Xiong, B. Xu, and T. Tan, "China Brain Project: Basic Neuroscience, Brain Diseases, and Brain-Inspired Computing," Neuron **92**(3), 591–596 (2016).
2. R. Chen, A. Canales, and P. Anikeeva, "Neural recording and modulation technologies," Nat. Rev. Mater. **2**(2), 16093 (2017).
3. G. K. Anumanchipalli, J. Chartier, and E. F. Chang, "Speech synthesis from neural decoding of spoken sentences," Nature **568**(7753), 493–498 (2019).
4. J. J. Jun, N. A. Steinmetz, J. H. Siegle, D. J. Denman, M. Bauza, B. Barbarits, A. K. Lee, C. A. Anastassiou, A. Andrei, C. Aydın, M. Barbic, T. J. Blanche, V. Bonin, J. Couto, B. Dutta, S. L. Gratiy, D. A. Gutnisky, M. Hausser, B. Karsh, P. Leochwitsch, C. M. Lopez, C. Mitelut, S. Musa, M. Okun, M. Pachitariu, J. Putzeyes, P. D. Rich, C. Rossant, W. L. Sun, K. Svoboda, M. Crandini, K. D. Harris, C. Koch, J. O'Keefe, and T. D. Harris, "Fully integrated silicon probes for high-density recording of neural activity," Nature **551**(7679), 232–236 (2017).
5. R. Bhandari, S. Negi, and F. Solzbacher, "Wafer-scale fabrication of penetrating neural microelectrode arrays," Biomed. Microdevices **12**(5), 797–807 (2010).

Optical Materials EXPRESS

6. J. Viventi, D. H. Kim, L. Vigeland, E. S. Frechette, J. A. Blanco, Y. S. Kim, A. E. Avrin, V. R. Tiruvadi, S. W. Hwang, A. C. Vanleer, D. F. Wulsin, K. Davis, C. E. Gelber, L. Palmer, J. Van der Spiegel, J. Wu, J. Xiao, Y. Huang, D. Cntreras, J. A. Rogers, and B. Litt, "Flexible, foldable, actively multiplexed, high-density electrode array for mapping brain activity in vivo," Nat. Neurosci. **14**(12), 1599–1605 (2011).
7. E. M. C. Hillman, "Optical brain imaging in vivo: techniques and applications from animal to man," J. Biomed. Opt. **12**(5), 051402 (2007).
8. X. Zhu, Y. Xia, X. Wang, K. Si, and W. Gong, "Optical Brain Imaging: A Powerful Tool for Neuroscience," Neurosci. Bull. **33**(1), 1–16 (2017).
9. M. R. Warden, J. A. Cardin, and K. Deisseroth, "Optical Neural Interfaces," Annu. Rev. Biomed. Eng. **16**(1), 103–129 (2014).
10. T. Chen, T. J. Wardill, Y. Sun, S. R. Pulver, S. L. Renninger, A. Baohan, E. R. Schreiter, R. A. Kerr, M. B. Orger, V. Jayaraman, L. L. Looger, K. Svoboda, and D. S. Kim, "Ultrasensitive fluorescent proteins for imaging neuronal activity," Nature **499**(7458), 295–300 (2013).
11. F. Sun, J. Zeng, M. Jing, J. Zhou, J. Feng, S. F. Owen, Y. Luo, F. Li, H. Wang, T. Yamaguchi, Z. Yong, Y. Gao, W. Peng, L. Wang, S. Zhang, J. Du, D. Lin, M. Xu, A. C. Kreitzer, G. Gui, and Y. Li, "A Genetically Encoded Fluorescent Sensor Enables Rapid and Specific Detection of Dopamine in Flies, Fish, and Mice," Cell **174**(2), 481–496.e19 (2018).
12. F. St-Pierre, J. D. Marshall, Y. Ying, G. Yiyang, M. J. Schnitzer, and M. Z. Lin, "High-fidelity optical reporting of neuronal electrical activity with an ultrafast fluorescent voltage sensor," Nat. Neurosci. **17**(6), 884–889 (2014).
13. E. J. Yoder and D. Kleinfeld, "Cortical imaging through the intact mouse skull using two-photon excitation laser scanning microscopy," Microsc. Res. Tech. **56**(4), 304–305 (2002).
14. D. A. Dombeck, A. N. Khabbaz, F. Collman, T. L. Adelman, and D. W. Tank, "Imaging Large-Scale Neural Activity with Cellular Resolution in Awake, Mobile Mice," Neuron **56**(1), 43–57 (2007).
15. J. M. Wilson, D. A. Dombeck, D. R. Manuel, R. M. Harris-Warrick, and R. M. Brownstone, "Two-photon calcium imaging of network activity in XFP-expressing neurons in the mouse," J. Neurophysiol. **97**(4), 3118–3125 (2007).
16. A. Li, H. Gong, B. Zhang, Q. Wang, C. Yan, J. Wu, Q. Liu, S. Zeng, and Q. Luo, "Micro-optical sectioning tomography to obtain a high-resolution atlas of the mouse brain," Science **330**(6009), 1404–1408 (2010).
17. K. Chung, J. Wallace, S. Kim, S. Kalyanasundaram, A. S. Andalman, T. J. Davidson, J. J. Mirzabekov, K. A. Zalocusky, J. Mattis, A. K. Denisin, S. Pak, H. Bernstein, C. Ramakrishnan, L. Grosenick, V. Gradinaru, and K. Deisseroth, "Structural and molecular interrogation of intact biological systems," Nature **497**(7449), 332–337 (2013).
18. F. Chen, P. W. Tillberg, and E. S. Boyden, "Expansion Microscopy," Science **347**(6221), 543–548 (2015).
19. H. Xu, L. Yin, C. Liu, X. Sheng, and N. Zhao, "Recent Advances in Biointegrated Optoelectronic Devices," Adv. Mater. **30**(33), 1800156 (2018).
20. B. A. Flusberg, E. D. Cocker, W. Piyawattanametha, J. C. Jung, E. L. M. Cheung, and M. J. Schnitzer, "Fiber-optic fluorescence imaging," Nat. Methods **2**(12), 941–950 (2005).
21. A. D. Mehta, J. C. Jung, B. A. Flusberg, and M. J. Schnitzer, "Fiber optic in vivo imaging in the mammalian nervous system," Curr. Opin. Neurobiol. **14**(5), 617–628 (2004).
22. W. Zong, R. Wu, Y. Hu, Y. Li, J. Li, H. Rong, H. Wu, Y. Xu, Y. Lu, M. Fan, Z. Zhou, A. Wang, H. Cheng, and L. Chen, "Fast High-resolution Miniature Two-photon Microscopy for Brain Imaging in Freely-behaving Mice at the Single-spine Level," Nat. Methods **14**(7), 713–719 (2017).
23. K. M. Tye, R. Prakash, S. Y. Kim, L. E. Fenno, L. Grosenick, H. Zarrabi, K. R. Thompson, V. Gradinaru, C. Ramakrishnan, and K. Deisseroth, "Amygdala circuitry mediating reversible and bidirectional control of anxiety," Nature **471**(7338), 358–362 (2011).
24. C. D. Harvey, C. Forrest, D. A. Dombeck, and D. W. Tank, "Intracellular dynamics of hippocampal place cells during virtual navigation," Nature **461**(7266), 941–946 (2009).
25. J. Ohta, Y. Ohta, H. Takehara, T. Noda, K. Sasagawa, T. Tokuda, M. Haruta, T. Kobayashi, Y. M. Akay, and M. Akay, "Implantable Microimaging Device for Observing Brain Activities of Rodents," Proc. IEEE **105**(1), 158–166 (2017).
26. L. V. Wang, H. I. Wu, and B. R. Masters, "Biomedical Optics, Principles and Imaging," J. Biomed. Opt. **13**(4), 049902 (2008).
27. S. C. Gebhart, W. C. Lin, and A. Mahadevan-Jansen, "In vitro determination of normal and neoplastic human brain tissue optical properties using inverse adding-doubling," Phys. Med. Biol. **51**(8), 2011–2027 (2006).
28. L. Wang, S. L. Jacques, and L. Zheng, "MCML—Monte Carlo modeling of light transport in multi-layered tissues," Comput. Meth. Programs Biomed. **47**(2), 131–146 (1995).
29. H. S. Meyer, D. Schwarz, V. C. Wimmer, A. C. Schmitt, J. N. D. Kerr, B. Sakmann, and M. Helmstaedter, "Inhibitory interneurons in a cortical column form hot zones of inhibition in layers 2 and 5A," Proc. Natl. Acad. Sci. U. S. A. **108**(40), 16807–16812 (2011).
30. C. Grienberger and A. Konnerth, "Imaging Calcium in Neurons," Neuron **73**(5), 862–885 (2012).
31. R. Fu, W. Luo, R. Nazempour, D. Tan, H. Ding, K. Zhang, L. Yin, J. Guan, and X. Sheng, "Implantable and Biodegradable Poly(l-lactic acid) Fibers for Optical Neural Interfaces," Adv. Opt. Mater. **6**(3), 1700941 (2018).
32. L. Lu, P. Gutruf, L. Xia, D. L. Bhatti, X. Wang, A. Vazquez-Guardado, X. Ning, X. Sheng, T. Sang, R. Ma, G. Pakeltis, G. Sobczak, H. Zhang, D. O. Seo, M. Xue, L. D. Chanda, X. Sheng, M. R. Bruchas, and J. A. Rogers, "Wireless optoelectronic photometers for monitoring neuronal dynamics in the deep brain," Proc. Natl. Acad. Sci. U. S. A. **115**(7), E1374–E1383 (2018).

Optical Materials EXPRESS

33. S. Herculano-Houzel, "The human brain in numbers: a linearly scaled-up primate brain," Front. Hum. Neurosci. **3**, 31 (2009).
34. M. Khorasaninejad and F. Capasso, "Metalenses: Versatile multifunctional photonic components," Science **358**(6367), eaam8100 (2017).
35. M. J. Nasse and J. R. C. Woehl, "Realistic modeling of the illumination point spread function in confocal scanning optical microscopy," J. Opt. Soc. Am. A **27**(2), 295 (2010).
36. H. Dana, B. Mohar, Y. Sun, S. Narayan, A. Gordus, J. P. Hasseman, G. Tsegaye, G. T. Holt, A. Hu, D. Walpita, R. Patel, J. J. Macklin, C. I. Bargmann, M. B. Ahrens, E. R. Schreiter, V. Jayaraman, L. L. Looger, K. Svoboda, and D. S. Kim, "Sensitive red protein calcium indicators for imaging neural activity," eLife **5**, e12727 (2016).